Analysis of rheology and wall depletion of microfibrillated cellulose suspension using optical coherence tomography

Janne Lauri, [1]

Antti Koponen, [2]✉

Phone +358 20 722 2717
Email Antti.Koponen@vtt.fi

Sanna Haavisto, [3,4]

Jakub Czajkowski, [1]

Tapio Fabritius, [1]

[1] Optoelectronics and Measurement Techniques Unit, Faculty of Information Technology and Electrical Engineering, University of Oulu, P.O. Box 4500, FI-90014 Oulu, Finland

[2] VTT Technical Research Centre of Finland Ltd, P.O. Box 10603, FI-40101 Jyväskylä, Finland

[3] Department of Physics, University of Jyväskylä, P.O. Box 35, FI-40014 Jyväskylä, Finland

[4] Spinnova Ltd., Asematie 11, 40800 Vaajakoski, Finland

Abstract

A rheometric method based on velocity profiling by optical coherence tomography (OCT) was used in the analysis of rheological and boundary layer flow properties of a 0.5% microfibrillated cellulose (MFC) suspension. The suspension showed typical shear thinning behaviour of MFC in the interior part of the tube, but the measured shear viscosities followed interestingly two successive power laws with an identical flow index (exponent) and a different consistency index. This kind of viscous behaviour, which has not been reported earlier for MFC, is likely related to a sudden structural change of the suspension. The near-wall flow showed existence of a slip layer of 2–12 μm thickness depending on the flow rate. Both the velocity profile measurement

and the amplitude data obtained with OCT indicated that the slip layer was related to a concentration gradient appearing near the tube wall. Close to the wall the fluid appeared nearly Newtonian with high shear rates, and the viscosity approached almost that of pure water with decreasing distance from the wall. The flow rates given by a simple model that included the measured yield stress, viscous behavior, and slip behavior, was found to give the measured flow rates with a good accuracy.

Keywords

Shear viscosity
Yield stress
Lubrication layer
Slip velocity
Velocity profile
Optical coherence tomography

Introduction

Recently, there has been a growing interest towards disintegrating pulp fibres to their elementary fibrils, thereby producing a renewable, recyclable and biodegradable raw stock for novel cellulosic materials. The disintegration can be performed using a combination of mechanical grinders, together with chemical or enzymatic treatments that typically yield an aqueous suspension of fibrils.

The dimensions of the produced fibrils, called micro (nano) fibrillated cellulose fibres (MFC), can be diverse: the length can vary from hundreds of nanometers to tens of micrometers (Jonoobi et al. 2015). Thus, the mechanical properties of MFC fibres and fibre suspensions are quite different from cellulosic pulp suspensions, which consist of macroscopic fibres. MFC fibres have a very high specific surface area, and ability to form a highly porous network. Due to a high aspect ratio of fibres and strong interfibrillar forces, MFC forms a highly entangled network already in very dilute aqueous suspensions. Furthermore, chemical properties of the MFC may vary greatly depending on the applied methods of disintegration and the source of the raw material (Kalia et al. 2014; Missoum et al. 2013).

The unique characteristics of MFC, combined with environmental friendliness, make MFC an interesting target for research. MFC has been found to have a potential in a wide spectrum of applications, such as strength agents in papermaking (Osong et al. 2016), barriers in cellulosic products (Lavoine et al. 2012), transparent and conductive composites for printed electronics (Hoeng et

al. 2016), rheology modifiers and stabilizers (Dimic-Misic et al. 2013), nanocomposites (Siró and Plackett 2010), and 3D printing (Markstedt et al. 2015; Shao et al. 2015).

A frequently noted issue in processing of MFC suspensions is their complex rheological behaviour. Rheological information is critical in the design and operation of e.g. pumping, mixing, storage, and extrusion processes. Thus, bulk rheology of MFC suspensions has been a popular subject of discussion (Naderi and Lindström 2015; Nazari et al. 2016; Kumar et al. 2016). Furthermore, much rheological research has been dedicated to characterization of MFC suspensions produced by diverse disintegration methods, as well as by using different sources of cellulosic fibres (Agoda-Tandjawa et al. 2010; Chen et al. 2013; Iotti et al. 2011; Lasseuguette et al. 2008; Pääkkö et al. 2007). The results have shown that MFC suspensions tend to form a strong gel, which shows yield stress, shear thinning, hysteresis, and thixotropy already in very low mass concentrations. In addition to the mass consistency, a strong relation between rheological parameters and pH of the suspension, together with presence of some additives has been reported (Pääkkö et al. 2007; Sorvari et al. 2014; Vesterinen et al. 2010). A recent study has shown that the dimensions of cellulosic elements as well as their surface character are important parameters, which affect the rheological behaviour of MFC significantly (Moberg et al. 2017).

Similarly, to pulp fibres or particle suspensions in general, MFC suspensions are also prone to wall depletion (Barnes 1995). The fibrils tend to migrate away from the walls of the conduit due to geometric effects and hydrodynamic lift forces. This phenomenon is not just of academic interest; it has also a significant practical relevance (Cloitre and Bonnecaze 2017). For example, in a pipe flow, the water-rich layer thus formed may lead to a significant *apparent wall slip*, which increases the volumetric flow rate of the MFC suspensions considerably (Haavisto et al. 2015). (Notice that in the literature, and in this paper, ‘apparent (wall) slip’ is for practical reasons usually called simply ‘(wall) slip’. When using a velocity profiling technology with too low spatial resolution, the velocity profile may apparently slip at the wall although the no-slip boundary condition still holds in a microscopic level. Moreover, in numerical analysis slip models are often used for describing the effect of wall depletion on macroscopic flow behaviour.) Furthermore, wall depletion affects the interpretation of rheometer data, as the measured result depends not only on the actual ‘bulk’ rheological properties, but also on the sometimes intricate boundary layer behaviour of the flow in the particular device being used (Haavisto et al. 2015; Karppinen et al. 2012; Kumar et al. 2016; Nazari et al. 2016). Especially low shear rates are prone to slip flow that can introduce a significant error in the rheological measurements (Nechyporchuk et al. 2014; Saarinen et al. 2014). When

performing rheological measurements with MFC, observations of apparent wall slip, and another complex rheological phenomenon, shear banding (Martoïa et al. 2015; Olmsted 2008), have, however, been discussed in relatively few studies.

Nowadays a quite established technique, optical coherence tomography (OCT) (Huang et al. 1991), has been demonstrated to accurately measure flow velocity of turbid and opaque fluid at the vicinity of the wall of the conduit (Wang et al. 1995). The opaque fluids have included e.g. Intralipid (Wang et al. 2004b; Yang et al. 2003), blood (Bukowska et al. 2013; Moger et al. 2004), and polymer and colloidal suspensions (Jia et al. 2009; Wang et al. 2004a). Recently, it has been shown that the OCT is a great tool to be used in rheological measurements (Harvey and Waigh 2011; Jaradat et al. 2012; Lauri et al. 2011a) and well suited to study the complex rheology of MFC suspensions (Haavisto et al. 2015; Saarinen et al. 2014; Salmela et al. 2013). The latest developments in OCT technique have combined a one-micron axial resolution with a high measurement speed and a sensitivity (Robles et al. 2011; Yadav et al. 2011), which enable very detailed studies of boundary layer dynamics of complex suspensions.

There are few studies where the dynamics of the depletion layer has been measured explicitly for MFC suspensions, and all of them have utilized OCT. (Saarinen et al. 2014) applied OCT in combination with a rheometer, but only for imaging purposes. (Salmela et al. 2013) measured the velocity profile close to the wall in a pipe flow, but quantitative analysis of rheology remained in a preliminary level. The emphasize of (Haavisto et al. 2015) was in demonstrating the use of OCT and pulsed ultrasound velocimetry for rheological characterization of MFC.

In this study, we use a combination of pipe flow and pressure loss measurement with a high-speed, sub-micron resolution OCT device for investigating the rheology and structure of a 0.5% MFC suspension. The goal is to fully utilize the capabilities of OCT in measuring high-resolution velocity profiles and to perform the rheological analysis rigorously. In addition to analysing the bulk rheology (yield stress and viscous behaviour), the wall layer dynamics of the suspension is studied in detail. The benefit of performing the rheological experiments in a real process geometry in a combination with an apparent slip measurement is demonstrated by comparing the results with earlier rheometer studies, and by introducing a simple flow model, that predicts the volumetric flow rate of the MFC suspension with a good accuracy.

Materials and methods

Microfibrillated cellulose

The microfibrillated cellulose samples were prepared from never dried bleached kraft birch pulp via grinding three times in a supermasscolloider (Masuko Sangyo, Japan). Prior to grinding, the pulp was changed to its sodium form and washed with deionized water to obtain an electrical conductivity less than 10 S/cm, according to a procedure introduced by (Swerin et al. 1990). The dry matter content after grinding was 2 wt%. For the rheological experiments, MFC samples were diluted with deionized water to mass concentration of 0.5 wt%. An image of the MFC fibers is shown in Fig. 1.

Fig. 1

An image of the microfibrillated cellulose used in this study. The distributions of length and width are very broad

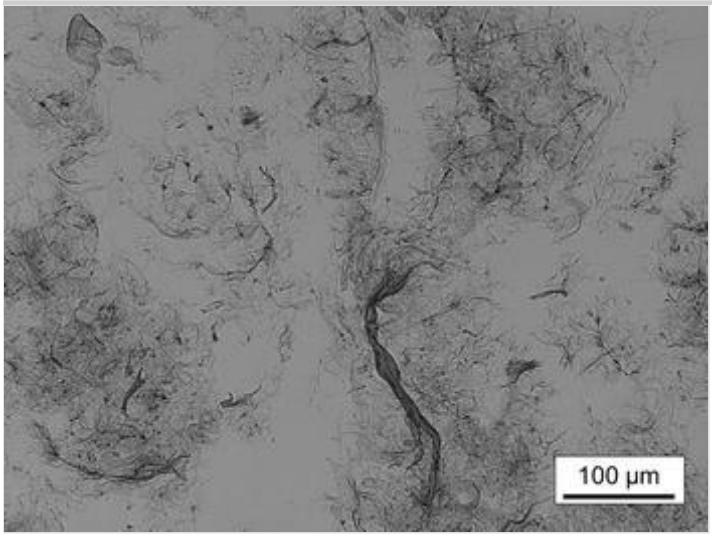

Optical coherence tomography

OCT is a light-based imaging method, which enables accurate non-contact measurement of a scattering material (Huang et al. 1991). OCT uses interference of a low coherence light to record depth-dependent reflectivity profile (A-scan). By lateral scanning and combining A-scans, 2D cross-sectional and 3D volumetric images can be generated. In addition to structural imaging, velocity information can be retrieved simultaneously–this imaging mode is often referred as Doppler OCT (Wang et al. 1995; Zhao et al. 2000). Doppler OCT enables a high-resolution measurement of velocity profiles close to a conduit's wall. Therefore, it is well suited to accurately study the boundary layer flow behaviour of complex fluids with appropriate optical properties (Bonesi et al. 2007; Lauri et al. 2011b; Wang 2004). In the case of flow measurements, a commonly used method is the so-called M-mode, in which the probing beam is held at the same location and data is acquired over a certain period with a constant sampling rate. In M-mode, faster transients can be observed and signal-to-noise-ratio is improved due to averaging. When OCT is combined with pressure loss (e.g. pipe

flow) or shear stress (e.g. rotational rheometers) measurements, velocity profiling (i.e. calculation of local viscosities of the studied fluid) becomes possible.

The laboratory-built spectral domain OCT device described in Refs. (Czajkowski et al. 2012; Lauri et al. 2015) was used in this study. This device has an axial resolution of 0.9 μm in water. A maximum scanning depth is 365 μm in water and consists of 1024 pixels resulting in a native pixel resolution of 0.36 μm. The experiments were done in M-mode and Doppler phase was calculated from a phase difference of adjacent A-scans (Yang et al. 2003; Zhao et al. 2000). An axial scan rate was set according to the current flow rate in order to avoid the 2π ambiguity in Doppler phase calculation. The set scan rates varied between 31 and 123 kHz (the maximum of the device). The Doppler phase, used in velocity calculation, was determined by calculating a histogram from 50,000 phases for each depth separately. The obtained histogram was fitted with a Gaussian distribution of which peak location indicated the value of the Doppler phase. The goodness of this fit can vary quite a lot but the fitting enables recovery of the centroid Doppler phase with a very good accuracy even in such cases where the signal-to-noise ratio is low. The obtained phases along the OCT beam were converted to axial velocities according to the normal procedure (Yang et al. 2003).

Pipe rheometer

The pipe rheometer configuration was similar to the one presented in (Haavisto et al. 2015; Salmela et al. 2013). The MFC sample was fed through an optical grade glass pipe with a length of 1440 mm, an inner diameter of D = 8.6 mm and a wall thickness of 2.5 mm (see Fig. 2). A plastic container with an inner diameter of 8.6 cm and volume of 1.3 l, filled with a sample, was connected to the glass pipe with a rubber hose having an inner diameter of 11.5 mm. The container was connected to a compressed air source via a pressure regulator. A steady and pulsation-free flow was induced by keeping a constant overpressure in the container. The flow rate was controlled and adjusted with both a manual valve after the glass pipe and the set overpressure. The highest applied overpressure equalled 1 bar. The mass flow rate was acquired with a computer controlled laboratory-scale and the corresponding pressure drop, was measured with a differential pressure sensor (2051, Emerson Process Management). The pressure sensor was connected with hoses into two holes (L1 and L3, see Fig. 2) having a diameter of 2 mm. The holes were drilled at a distance L = 840 mm apart and the first one was located at 450 mm from the inlet. The experiments were performed at the room temperature of 22 degrees (water viscosity was thus 0.95 mPas).

Fig. 2

A schematic of the pipe rheometer

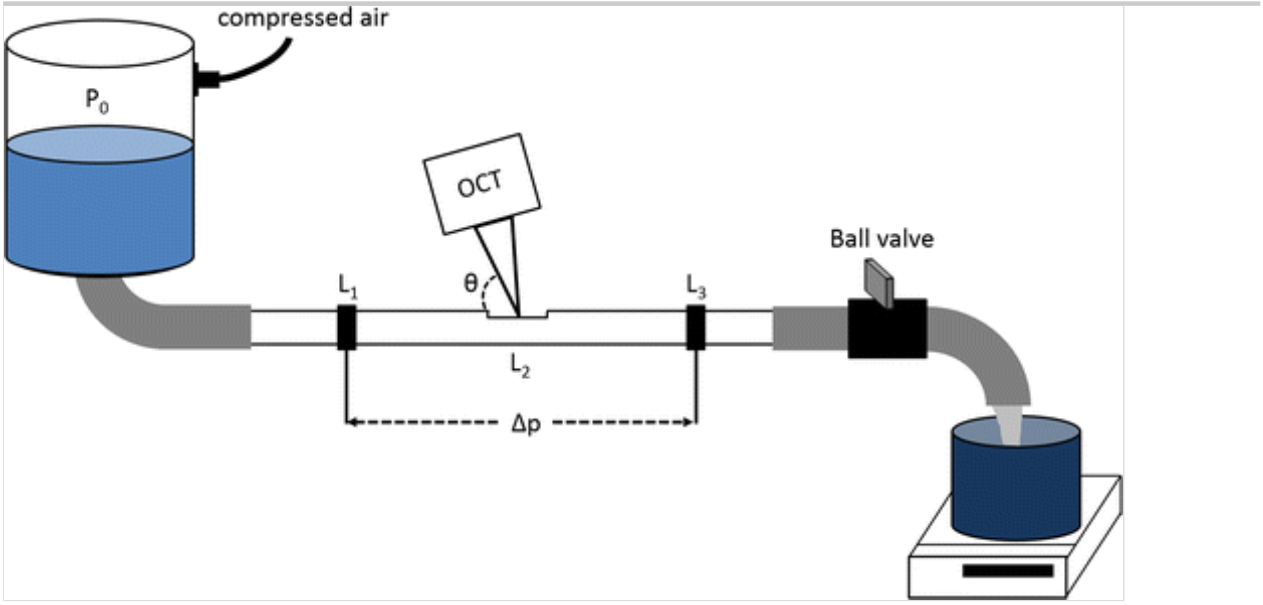

The OCT imaging was performed at the distance of 950 mm (L2, see Fig. 2) from the pipe inlet. The Doppler angle θ was 85.6 degrees. A flat window was grind to the pipe surface to reduce specular reflections from the outer surface of the pipe and to improve the dynamic range of the image. This also reduced the degradation of the axial resolution due to strong dispersion caused by the glass wall. The residual dispersion mismatch between the interferometer arms was compensated by placing a glass slide within the reference arm. For each flow rate, 50,000 A-scans were acquired using OCT in less than 1.7 s (depending on the scanning frequency). The time to record the mass flow rate and the pressure drop varied between 5 and 20 s. At the highest flow rate, the container was emptied during a single measurement.

Results

Pressure loss

Figure 3 shows the pressure gradient of the 0.5% MFC suspension as the function of the flow rate in the pipe. At low flow rates (below 30 ml/min, see the inset picture) the MFC suspension behaves like a Bingham fluid: it remains stationary until the pressure gradient exceeds 500 Pa/m, above which the pressure gradient depends linearly on the flow rate. With higher flow rates, the slope of the flow rate-pressure gradient curve decreases rapidly with increasing flow rate indicating that the rheological behaviour of the MFC suspension is shear thinning.

Fig. 3

Pressure gradient as a function of flow rate. The dashed line is the power-law fit $\nabla P = KQ^n$ (with coefficients K = 470, n = 0.36). The solid line is a linear fit to the 6 lowest flow rates

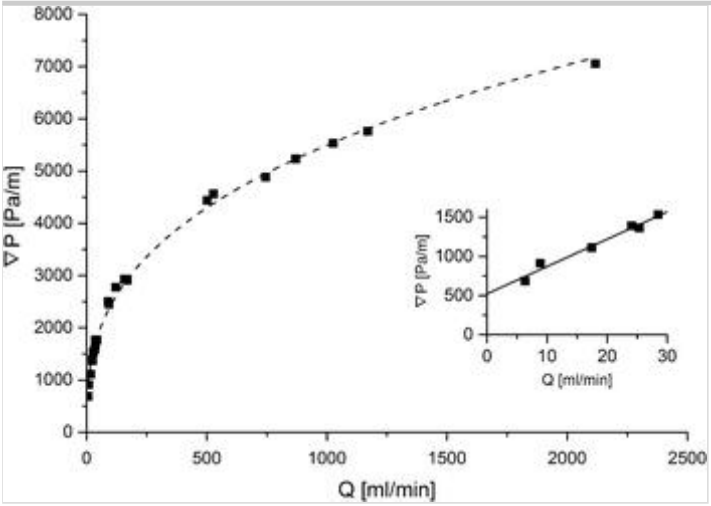

During the flow of suspension, the wall shear stress is $\tau_w = D\nabla P/4$, where D is the diameter of pipe and ∇P is the pressure gradient in the pipe. The maximum wall shear stress of a suspension, τ_{max}, is defined as the threshold value of the wall shear stress, above which the contact between the tube wall and the suspension bulk is lost. In these experiments, the maximum wall shear stress was determined from the intercept of the pressure gradient axis with a linear fit to the 6 lowest flow rates (see the inset in Fig. 3). The obtained value τ_{max} = 1.1 Pa coincides with earlier measurements in a vane-in-cup rheometer with a polymethyl methacrylate (PMMA) surface for an identical MFC suspension (Saarinen et al. 2014).

Measured velocity and amplitude signals

Figure 4 shows an example of the measured velocity and amplitude signals at the flow rate of 503 ml/min. Velocity data could be obtained, in the best case, up to 200 μm from the pipe wall, excluding the immediate vicinity of the wall. The closest point relative to the pipe wall having reliable velocity data was estimated to be 2 μm, below which the profiles were affected by the signal originating from the wall. This distance is approximately two times the axial resolution of the used OCT. The loss of resolution at the wall is most likely due to the residual dispersion mismatch between the interferometer arms.

Fig. 4

An example of a measured flow velocity profile (Q = 503 ml/min) together with a corresponding OCT amplitude signal

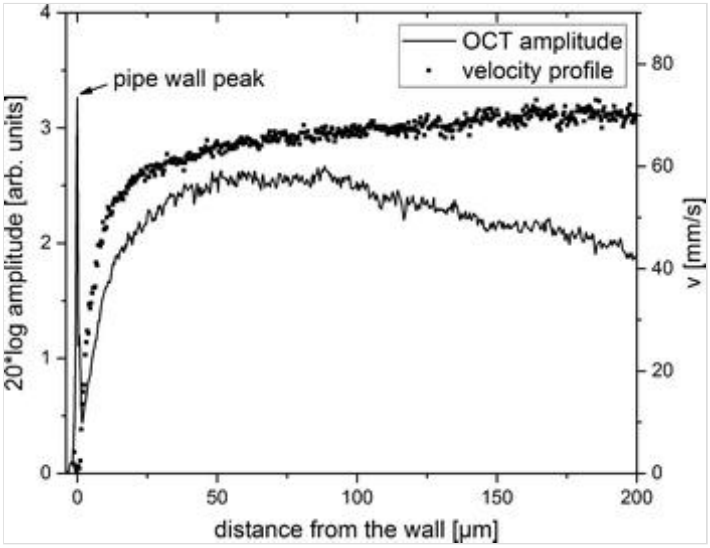

Figure 5 shows the velocity profiles at various flow rates, as measured by the OCT. Close-up graphs of the profiles in the close proximity to the wall are also shown. For the lowest flow rate of 9 ml/min, the velocity profile corresponds to a pure plug flow in the whole pipe, excluding a yielding marginal wall layer of a few microns in thickness. At higher flow rates, the yielding area widens and the velocity profiles consist of three distinctive parts. In the outer (bulk) region, at the distances greater than 15 µm, the slope of the profile (shear rate) is small. In the region of 2–15 µm the velocity profile is rather steep and approaches zero towards the wall. In the immediate vicinity of the wall (distance 0–2 µm) the velocity drops abruptly to zero. The most natural explanation for the observed behaviour of the velocity profile is a development of a consistency profile in the pipe when the distance from the wall is smaller than 15 µm.

Fig. 5

Examples of the flow velocity profiles (a) and a close-up at the wall (b)

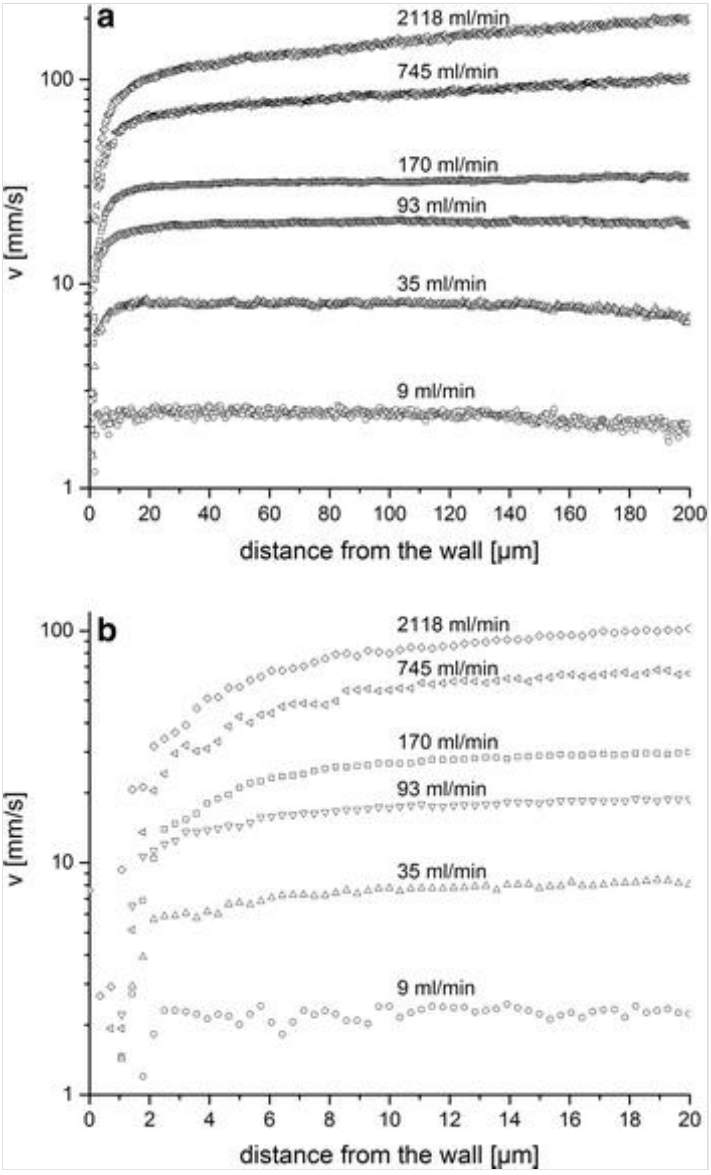

Parametrization of the velocity profiles

The measured velocity profiles were fitted by the empirical formula

$$u(y) = \dot{\gamma}_w^a y + u_s^a \left(1 - e^{-\frac{y}{\lambda_w}}\right) + u_s, \qquad 1$$

where y is distance from the wall and $\dot{\gamma}_w^a$, u_s^a, u_s and λ_w are free parameters (see Fig. 6). Parameter $\dot{\gamma}_w^a$ is the apparent shear rate at wall, u_s^a and u_s are the apparent slip velocities, and λ_w is the characteristic thickness of the apparent slip layer. The fitting was carried out in the profile region starting from 2 µm. The width of the fitting region varied between 125 and 185 µm, being wider at the higher flow rates. At further distances from the wall, poor signal-to-noise-ratios (due to the attenuation of the optical signal) and aliasing led to disturbed velocity profiles. This caused the velocity and amplitude profiles to turn downwards (see flow rates 9 and 35 ml/min in Fig. 5a, and the amplitude curve in Fig. 4). The fitted parameters together with the corresponding flow rates and wall shear stresses are shown in the Table 1.

Fig. 6

Example of a fitted velocity profile Eq. (1) to the measured velocity values at Q = 2118 ml/min (solid curve). Also shown are the four free fitting parameters $\dot{\gamma}_w^a$, u_s^a, u_s and λ_w

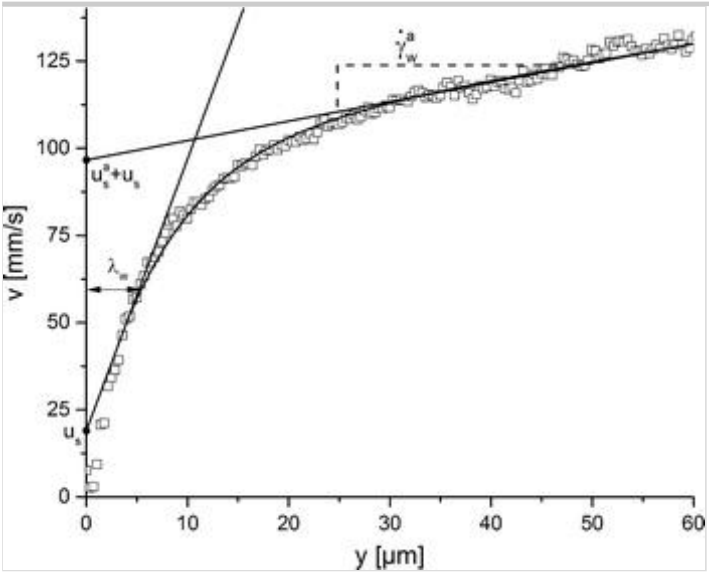

Table 1

Flow rates, wall shear stresses, and corresponding fitting parameters for Eq. (1)

Q (ml/min)	τ_w (Pa)	$\dot{\gamma}_w^a$ (1/s)	u_s^a (mm/s)	u_s (mm/s)	λ_w (µm)
6	1.5	0	0.6	1.3	3.0
9	2.0	0	0.3	2.0	6.5
17	2.4	0	2.1	2.4	6.6
24	3.0	0	2.2	4.0	9.4
25	2.9	1	2.4	3.6	6.6
29	3.3	4	2.2	4.4	5.1
35	3.4	0	4.4	3.6	4.0
37	3.6	2	4.0	5.1	8.6
37	3.8	26	3.5	4.3	6.3
42	3.8	0	4.3	4.5	6.1
93	5.3	10	9.9	9.5	6.9
122	6.0	14	16.1	7.5	5.7
158	6.3	17	15.8	11.8	5.2
170	6.2	17	28.7	1.3	4.6

Q (ml/min)	(Pa)	(1/s)	(mm/s)	(mm/s)	(µm)
503	9.5	58	54.2	6.4	7.5
528	9.8	69	54.7	3.7	6.4
745	10.5	177	60.4	5.7	6.4
870	11.2	228	67.4	1.0	5.4
872	11.9	320	70.8	0.7	5.2
1026	11.9	249	69.5	8.7	7.2
1170	12.4	296	73.8	4.5	5.8
2118	15.2	508	86.1	13.3	7.8

Notice that Eq. (1) is almost identical to the one proposed for a more coarse MFC suspension in (Salmela et al. 2013). However, here an additional (slip) parameter u_s is needed. Parameter u_s accounts for the very high slope of the velocity curves (see Fig. 5b) in the immediate vicinity of the pipe wall (distance from the wall below 2 µm). It seems that the whole wall depletion area consists in this case of two regions: when going from the bulk region to the wall there is first a region where the consistency decreases gradually. This is reflected in the smoothly increasing slope of the velocity profile. Then, when the distance from the wall is below 2 µm, the consistency drops very quickly. With the current axial resolution of the used OCT setup, the best approximation for the velocity profile there is a linear profile $v(y)$, for which $v(0) = 0$ and $v(2\ \mu m) = u(2\ \mu m)$. With higher wall shear rates, this area became almost particle free, which was reflected in the fluid viscosity that reached that of pure water (see Fig. 10).

Yield stress

Static yield stress, $\tau_{y,s}$, is a material property of viscoplastic fluids defined as the stress at which the material begins to deform plastically. Prior to the yield point, the material deforms elastically returning to its original shape, when the (applied) stress is relaxed. Above the yield point, some structural changes are permanent and non-reversible. Dynamic yield stress, $\tau_{y,d}$, is the minimum stress required for maintaining the flow. The static yield stress is most applicable when looking at initiating flow in a material, for example, in pumping. Dynamic yield stress values are often smaller than static, and more applicable in applications for maintaining or stopping flow after initiation. Static yield stress is measured in a rheometer either by a start-up of a steady shear experiment or by gradually increasing the stress as a function of time and observing at which point the

suspension starts to yield (Cheng 1986; Derakhshandeh et al. 2010). Dynamic yield stress values can be determined from rheometric measurements by fitting a model to the measured shear stress–shear rate data points. (Dimic-Misic et al. 2016)

In a pipe geometry, the dynamic yield stress can be estimated directly from the measured velocity profile by determining the radial position where the suspension plug breaks (Haavisto et al. 2011; Raiskinmäki and Kataja 2005; Wiklund et al. 2006). In our case, this is not feasible, as no velocity data is available from the interior parts of the pipe. We can instead plot the fitting parameter $\dot{\gamma}_w^a$ (apparent shear rate at wall) as a function of the wall shear stress τ_w, to determine at which wall shear stress parameter $\dot{\gamma}_w^a$ becomes non-zero (see Fig. 7). However, as we see in Fig. 7, an exact threshold cannot be observed. There is instead a finite shear stress region of ca. 3–4 Pa where $\dot{\gamma}_w^a$ has a large variation. The static yield stress $\tau_{y,s}$ = 3.4 Pa, measured in (Saarinen et al. 2014) for an identical suspension in a vane-in-cup rheometer, is in the middle of this region.

Fig. 7

Dynamic yield stress can be estimated by plotting the fitting parameter $\dot{\gamma}_w^a$ (the slope of the velocity profile in the bulk region) as a function of the wall shear stress. The dashed lines depict the stress region where yielding ends/begins. (Notice that in the case marked with the open square the apparent shear rate $\dot{\gamma}_w^a$ was for an unexplained reason clearly bigger than expected, although the pressure loss and the velocity profile close to the wall were consistent with the other measurement points)

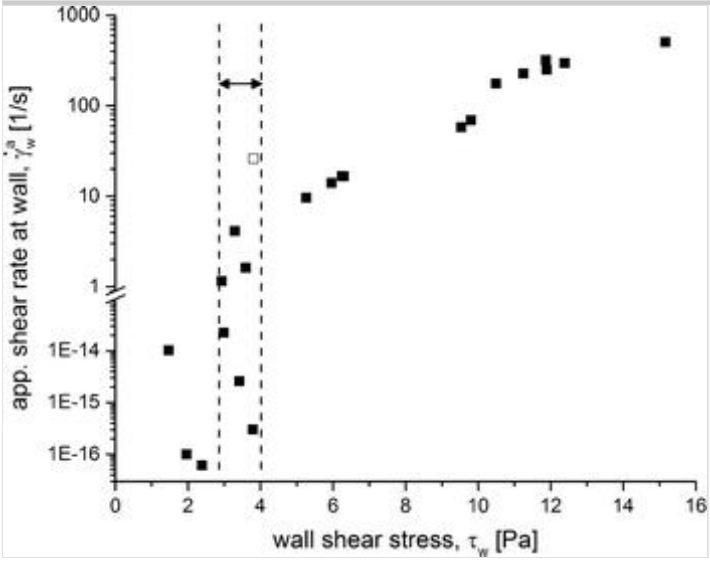

The lack of a distinct yield stress threshold in Fig. 7 is probably due to fluctuations around a yield point through continuous break-up and recovery of

the network structure combined with a limited measurement time. Such fluctuations may be caused by small variations in shear history and a non-homogeneous floc structure of the sample suspension. Their effect could be minimized by using longer measurement times and/or repeating the measurement several times.

As discussed above, the dynamic yield stress, $\tau_{y,d}$, of the suspension can often be determined by analyzing its shear stress behavior with a rheological model. Here the most natural candidate for such an analysis is the Herschel–Bulkley model, $\tau = \tau_{y,d} + K\dot{\gamma}^n$. However, a fit of this model to the measurement points 4 Pa < τ_w < 10 Pa gives $\tau_{y,d} \approx 0$. Another commonly used viscosity model for viscoplastic fluids is the Casson model, $\tau^{0.5} = \tau_{y,d}^{0.5} + a\dot{\gamma}^{0.5}$ (Barnes et al. 1989). A fit with this model gives $\tau_{y,d} = 3.4$ Pa, which is remarkably equal to the static yield stress measured by (Saarinen et al. 2014). As the dynamic and static yield stresses are here equal, we will talk simply about yield stress, τ_y, below.

Apparent slip velocity

As seen in Fig. 5a, the measured velocity profiles include a narrow near-wall region of the order of 15 μm, where the velocity profile is very steep and decreases rapidly to zero. When measured with a lower resolution technology, such as ultrasound or NMRI, the velocity profile would appear to slip at the wall with the slip velocity of $v_s = u_s^a + u_s$ thus apparently breaking the no-slip boundary condition.

We see in Table 1, that u_s and u_s^a behave differently as a function of wall shear stress. The slip velocity u_s^a, which is caused by the gradually decreasing MFC concentration profile when going from the bulk region to a 2 μm distance from the

wall, increases approximately monotonously when the wall shear stress increases. The slip velocity u_s, which is caused by the 2 μm thick low-consistency layer in the very vicinity of the wall, increases approximately monotonically as a function of wall shear stress until it exceeds 6 Pa. With higher wall shear stress values of u_s appears to fluctuate around 6 mm/s– probably due to sensitivity of fitting to small deviations of the measured velocity profile. The contribution of u_s and u_s^a to the total slip velocity are comparable when the wall shear stress is below 6 Pa. With higher wall shear stress u_s^a dominates the slip behaviour of the MFC suspensions.

Figure 8a shows the total slip velocity v_s as a function of the wall shear stress. As expected (Cloitre and Bonnecaze 2017), the slip velocity follows a power law

$$v_s = S\tau_w^m \quad (2)$$

with coefficients $S =$ 8.3 × 10^{-4} and $m =$ 1.84. The contribution of the slip velocity to the total volumetric flow is shown in Fig. 8b. The slip flow is seen to dominate the volumetric flow with small wall shear stress and it is significant also with the highest shear stresses. As a comparison, the relative slip for an identical MFC suspension on a stationary wall of a cylindrical rheometer geometry (Saarinen et al. 2014) is also shown in Fig. 8b. The relative slip in the pipe and the rheometer are qualitatively rather similar: the relative slip, e.g., drops in both cases abruptly, when the yield stress of the MFC suspension is exceeded.

Fig. 8

a) The slip velocity $v_s = u_s + u_s^a$ as a function of wall shear stress. A fit of a power-law $v_s = S\tau_w^m$ (with coefficients $S =$ 8.3 $\times 10^{-4}$ and $m =$ 1.84) is shown with a solid line. b) The contribution of slip velocity to the total volumetric flow as a function of the wall shear stress. As a comparison, the relative slip for an identical MFC suspension on a stationary wall of a cylindrical rheometer geometry is shown (Saarinen et al. 2014). The dashed line shows the yield stress τ_y = 3.4 Pa of the suspension

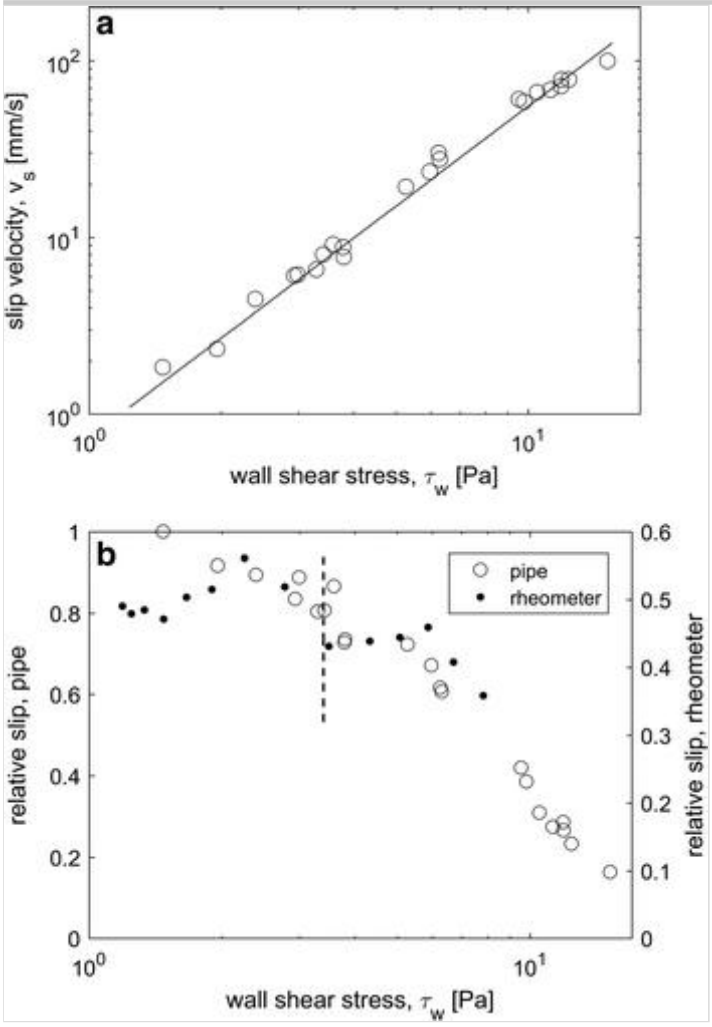

The thickness of the apparent slip layer

We see in Table 1 that the width of the fitted apparent slip layer, λ_w, fluctuates quite a lot especially below the yield stress. The fluctuations are likely caused by the sensitivity of fitting to small deviations of the measured velocity profile. It is likely, that λ_w is approximately constant–of the order of 6 μm. This conclusion is substantiated by the fact that when working on (Salmela et al. 2013) we found that the width of the fitted slip layer, λ_w was approximately constant for a 0.4% suspension of a commercial MFC (Celish® KY-100G, Daicel Chemical Industries).

However, the quantitative effect of the wall boundary layer on the slip flow and the flow rate depends also on the intensity of the depletion. The thickness of a water-rich layer that has real contribution to the apparent slip can be estimated e.g. by calculating the distance from the wall, below which the velocity profile $v(y)$ deviates more than a fraction β from the bulk velocity profile $v(y) = v_s + y\dot{\gamma}_w^a$. The results for $\beta = 0.2$ are shown in Fig. 9. We see, that increases from 2 to 12 μm with increasing wall shear stress. This suggests, that the slip layer is indeed due to wall depletion caused by hydrodynamic lift forces and is not e.g. due to geometrical restrictions on MFC flocs.

Fig. 9

The thickness of the water-rich layer that has real contribution to the slip as a function of wall shear rate (squares). The dashed line shows a linear fit to the plotted points

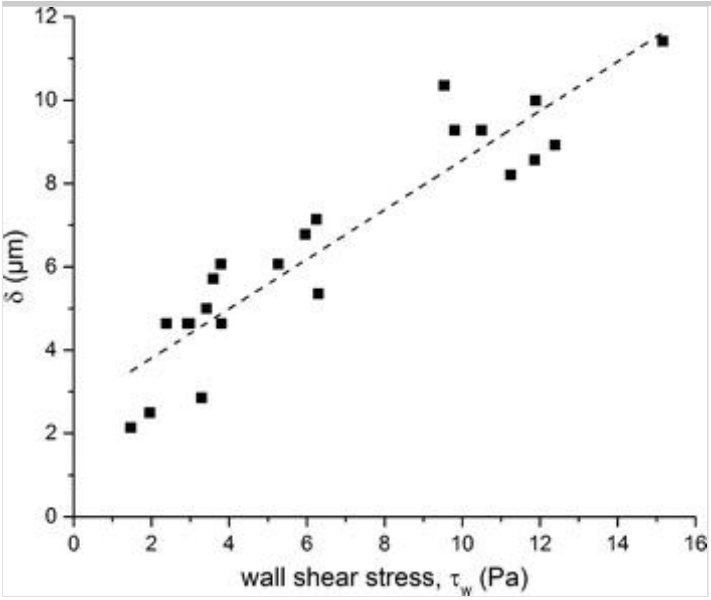

An often-used method for estimating the thickness of the apparent slip layer is to assume that all the slip takes place in a layer of pure water (Cloitre and Bonnecaze 2017). In such a case, the thickness of the pure water *effective slip layer* is

$$\delta_{\text{eff}} = \frac{\mu_0 v_s}{\tau_w}, \tag{3}$$

where μ_0 is the viscosity of water. By substituting Eqs. (2)–(3) one gets

$$\delta_{\text{eff}} = \mu_0 S \tau_w^{0.84}, \tag{4}$$

where $S = 8.3 \times 10^{-4}$. The thickness of the effective slip layer depends thus approximately linearly on the wall shear stress, and varies between 1 and 8 μm. Equation (4) can also be written in the form

$$\delta_{\text{eff}} = \mu_0 S' v_s^{0.46}, \tag{5}$$

where S' = 0.021.The comparison of our results with those found in literature is not straightforward as the MFC type, consistency, and the flow rate/shear rate regions vary. (Kumar et al. 2016) studied flow of a 1% MFC suspension in a 2 mm pipe. They obtained δ_{eff} = 10 μm with their lowest slip velocity of 130 mm/s, which is only slightly outside of our measurement range. Equation (5) gives for this slip velocity δ_{eff} = 8 μm. (Nazari et al. 2016) studied 1% MFC with a parallel plate geometry. They obtained with the shear rates 200 and 500 1/s the values 6 and 16 μm for δ_{eff}; our corresponding values are 6 and 8 μm. The order of our slip measurements agrees thus well with earlier results.

Viscosity

Figure 10 shows the viscosity of the MFC suspension as a function of shear stress at various distances from the wall. The viscosities have been calculated for $y > 2$ μm from the formula

$$\mu(y) = \frac{\tau(y)}{\dot{\gamma}(y)}, \tag{6}$$

where y is the distance from the wall,

$$\tau(y) = \tau_w (R - y)/R \tag{7}$$

is the local shear stress, and $\dot{\gamma}(y)$ is the shear rate, which is obtained by substituting the fitting parameters of Eq. (1) to the formula

$$\dot{\gamma}(y) = \frac{du}{dy} = \dot{\gamma}_w^a + \frac{u_s^a}{\lambda_w} e^{(-y/\lambda_w)}. \quad 8$$

The average viscosity in the region of 0–2 μm has been calculated using the formula

$$\mu_w = \tau_w \frac{y_w}{u(y_w)}, \quad 9$$

where τ_w is the wall shear stress, y_w = 2 μm is the distance from the wall, and $u(y_w)$ is obtained from Eq. (1).

Fig. 10

Viscosity as a function of shear stress at various distances from the wall. The viscosities have been calculated with Eqs. (6) and (9). The dashed line shows the viscosity of pure water 0.95 mPas at the measurement temperature of 22 °C

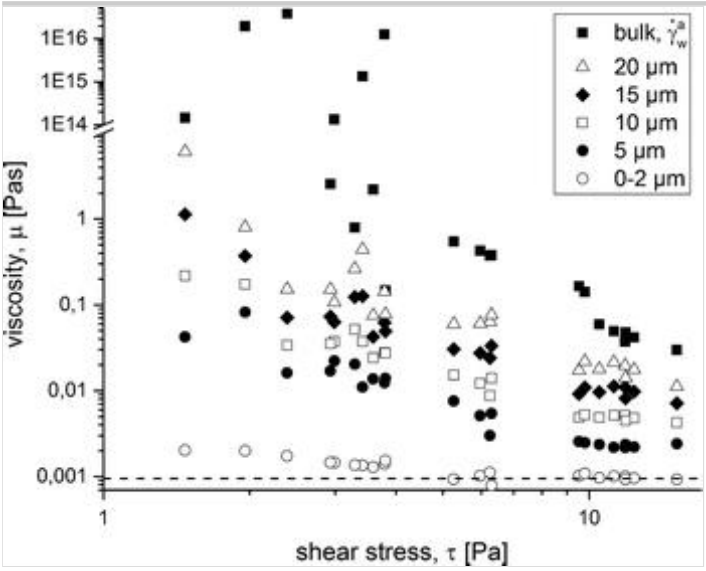

Figure 10 shows that the MFC suspension is a shear thinning fluid at most distances from the wall. This behaviour is typical for fibre suspensions but the root cause of the shear thinning of these materials is not yet fully understood. It has been found that mechanical contacts without or with friction are not enough to lead to a shear rate dependent viscosity–shear thinning is probably related to adhesive contacts between the fibres that are broken by the shear forces when the shear rate increases (Bounoua et al. 2016; Petrich et al. 2000).

In Fig. 10, at the given shear stress, the viscosity is always smaller closer to the wall. This is obviously due to the development of a MFC concentration gradient at the wall. Closer examination of the wall layer shows that towards the wall, with highest shear rates, the value of viscosity becomes independent of shear rate and approaches a constant value close to that of water, i.e. μ–1 mPas. Wall

depletion is then strong enough to remove all fibrils from the vicinity of the wall.

Figure 11 shows the bulk viscosity of the MFC suspension as a function of shear rate. Only those data points have been included, where the wall shear stress clearly exceeds the yield stress. As a comparison, data for an identical suspension obtained from a cylindrical rheometer geometry with a 1.0 mm gap is also shown (Saarinen et al. 2014). We see in Fig. 11 that the pipe and rheometer data agree very well when shear rate exceeds 100 1/s. With smaller shear rates, the viscosities are 30–50% bigger in the pipe than in the rheometer. This is likely due to slip flow at the walls of the rheometer cylinders, which, unlike in our case, was not eliminated in the rheological analysis.

Fig. 11

The bulk viscosity of the MFC suspension as a function of shear rate. The rheometer data for an identical MFC suspension has been taken from Ref. (Saarinen et al. 2014). The dashed lines show fits of the power law μ = K $\dot{\gamma}^n$ to the two sets of the pipe flow data

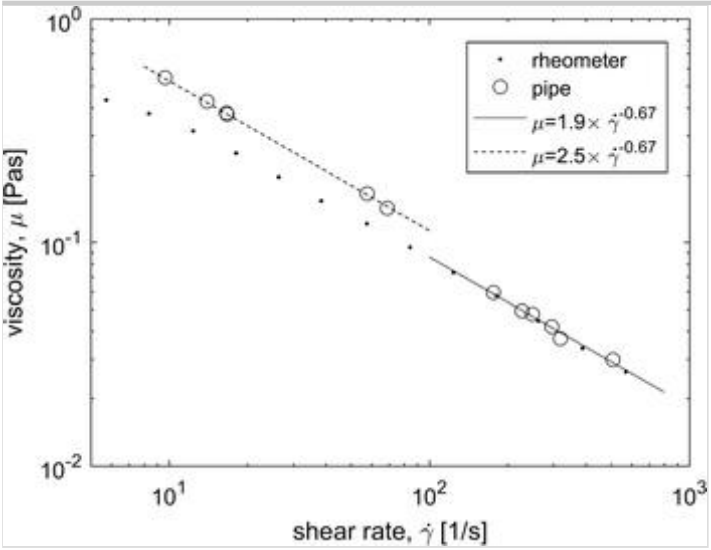

As we see from Fig. 11, the bulk viscosity of the MFC suspension can be written as

$$\mu = \begin{cases} 2.5 \times \dot{\gamma}^{-0.67}, & \tau < \tau_{\mathrm{tr}} \\ 1.9 \times \dot{\gamma}^{-0.67}, & \tau > \tau_{\mathrm{tr}} \end{cases}. \qquad 10$$

Figure 10 shows that the transition region between the two power laws is rather narrow; it takes place when the wall shear stress is between 9.8 and 10.4 Pa (we use below the value τ_{tr} = 10 Pa). To our knowledge, this kind of viscosity behavior has not been reported earlier for MFC suspensions. Such abrupt change

in the rheological behavior of the MFC suspension must be related with a sudden structural change in the suspension, e.g. in fibre orientation (Mykhaylyk et al. 2016) and/or flocculation (Bounoua et al. 2016). However, more data is needed to be able to conclude an exact cause for the abrupt change.

Calculating the flow rate

For a pipe flow of a power-law fluid one can calculate the (Metzner-Reed) Reynolds number with the formula presented in (Metzner and Reed 1955). As input parameters, the formula needs the yield stress of the fluid and the parameters of the power law. With the highest flow rate of 2118 ml/min, the Reynolds number is 40. The hydrodynamic entrance length of the suspension, $L_h/D = 0.05\mathrm{Re}$ (Bergman and Incropera 2011), is then two pipe diameters. The flow is thus laminar and fully developed in the whole measurement section.

For laminar and fully developed pipe flow of a suspension, quantitative flow rate prediction necessitates the knowledge of the yield stress of the suspension (see Fig. 7), its slip behaviour as a function of wall shear stress [see Fig. 8a and Eq. (2)] and its viscous behaviour as a function of shear rate [see Fig. 11 and Eq. (10)]. The flow rate of the suspension as a function of the wall shear stress is then obtained from the integral

$$Q = \int_0^R 2\pi(v + v_s) y \, dy \tag{11}$$

where

$$v = \int_0^y \frac{\tau}{\sqrt[n]{K\tau^{n-1}}} dy, \quad \text{when } 0 \le y \le y_y; v = \int_0^{y_y} \frac{\tau}{\sqrt[n]{K\tau^{n-1}}} dy, \quad \text{when } y_y \le y \le R.$$

Above τ is the (local) shear stress obtained from Eq. (7), and $y_y = R\left(1 - \frac{\tau_y}{\tau_w}\right)$ is the distance from the wall, where the shear stress equals the yield stress. Notice, that because the viscous behaviour is obtained from a combination of two power laws, n and K depend explicitly on τ and thus implicitly on y. Figure 12 compares the flow rates given by Eq. (11) with the flow rate measurements. We see, that there is a good agreement between them. The calculated flow rate deviates from the measured flow rate on the average only 12%, even though the span of flow rates is almost three orders of magnitude. When the rotational rheometer data shown in Fig. 11 was used in the flow rate calculations the error was on the average two times bigger. This result verifies

that the observed behaviour of viscosity Eq. (10) is real, and not an irregularity due to the close presence of the pipe wall in the (rheological) OCT measurements. As the flow rate measurement is independent from the pressure loss and OCT measurements, this result also confirms the accuracy of the used rheometric measurement setup.

Fig. 12

The measured and calculated flow rates for different wall shear stresses. Some measurement points have been combined for readability

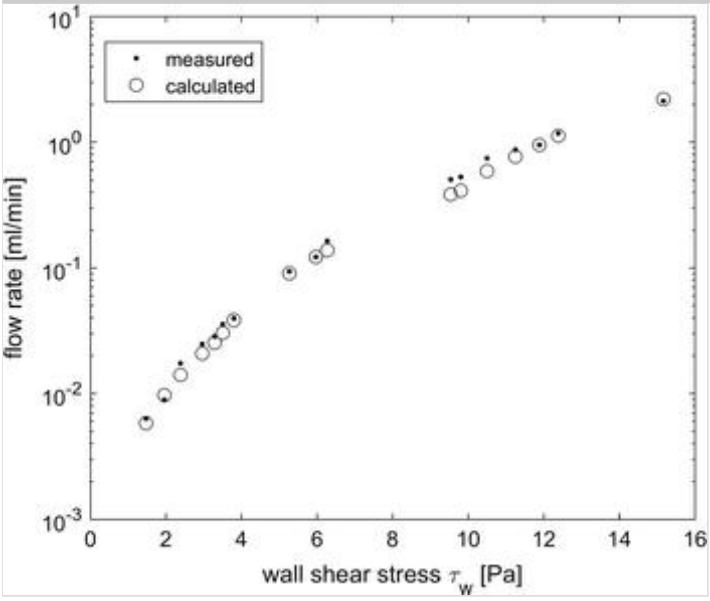

Conclusions

In this work, a sub-micron resolution optical coherence tomography device was successfully used together with a pipe rheometer to obtain the flow velocity profiles at the close vicinity of the pipe wall for rheological analysis of a 0.5% MFC suspension. The bulk behaviour of the studied MFC suspension showed typical shear thinning (power-law) behaviour in the interior part of the tube while the near-wall flow showed the existence of a 2–12 μm thick depletion layer. Both the velocity profile measurement and the amplitude data obtained with OCT indicated that this apparent slip layer was related to the concentration gradient appearing near the tube wall. The apparent slip flow due to the depletion layer was significant: with the lowest wall shear rates, it dominated the flow rate and its contribution was still 20% even with the highest flow rates used in this study. Close to the wall, the fluid appeared nearly Newtonian with high shear rates, and the viscosity of the fluid approached then even that of pure water with a decreasing distance from the wall.

There appeared to be a transition zone (around the wall shear stress of 10 Pa), where the quantitative behaviour of the suspension changed. The measured bulk

viscosities split there into two power laws that had the same flow index (exponent) but a different consistency index. To our knowledge such behavior, which must be related with a sudden structural change of the suspension, has not been reported earlier for MFC suspensions.

Comparison of the present results for yield stress, viscosity, and slip flow were performed with earlier measurements done with a rotational rheometer for an identical MFC suspension. It was found that rotational rheometers should not be used blindly for a quantitative analysis of real life processes. While there was an excellent agreement between the viscosities given by the pipe and the rheometer with high shear rates, the rheometer viscosities were 30–50% too small with low shear rates. This discrepancy was probably due to apparent slip flow, which was not eliminated in the analysis of the rheometer data. The slip results agreed reasonably well with each other, which implies that they could be applied also for other flow geometries. This possibility should be confirmed with boundary layer measurements using more complicated flow geometries.

In the literature, the hypothesis of an existence of a pure water slip layer is often made without direct quantitative measurements. Due to the high resolution of the used OCT, we were able to measure the velocity profile at the wall explicitly. We then showed that while the assumption of pure water layer can be useful for analysis purposes, it could be in reality very thin or even nonexistent.

The flow rates given by a simple model, that included the measured yield stress, viscous behavior, and slip behavior, was found to give the measured flow rates with a good accuracy. As well as confirming the reliability of the measurement setup, this result demonstrated the value of performing rheological experiments in a real process geometry together with slip flow measurements. The rheometric data presented in this paper data can also be useful in developing more fundamental models for the flow of MFC suspensions.

These experiments were performed for a fully developed flow. As a future work, it would be of interest to investigate the development of the boundary layer in the hydrodynamic entrance region of the pipe, since some real-world processes might not operate in a steady state.

We can conclude that a pipe rheometer equipped with an OCT device is a useful tool for flow and rheology measurements of MFC suspensions. It enables not only the analysis of the rheological (bulk) behaviour of the suspension in a realistic flow geometry, but gives also simultaneously information on the wall layer dynamics, both of which are needed for analysing and solving practical

fluid flow related problems. This approach would be useful also for rotational rheometers, to eliminate the effect of slip on the rheological analysis.

Acknowledgments

Academy of Finland (project Rheological Properties of Complex Fluids) is gratefully acknowledged for supporting this work. We also want to thank senior research technician Ulla Salonen for the photograph of the MFC fibers (Fig. 1), and senior scientist Panu Lahtinen for preparing the MFC.

References

Agoda-Tandjawa G, Durand S, Berot S, Blassel C, Gaillard C, Garnier C, Doublier J (2010) Rheological characterization of microfibrillated cellulose suspensions after freezing. Carbohydr Polym 80:677–686. doi:10.1016/j.carbpol.2009.11.045

Barnes HA (1995) A review of the slip (wall depletion) of polymer solutions, emulsions and particle suspensions in viscometers: its cause, character, and cure. J Non Newtonian Fluid Mech 56:221–251. doi:10.1016/0377-0257(94)01282-M

Barnes HA, Hutton JF, Walters K (1989) An introduction to rheology. Elsevier, Amsterdam

AQ1

Bergman TL, Incropera FP (2011) Fundamentals of heat and mass transfer. Wiley, Hoboken

Bonesi M, Churmakov D, Meglinski I (2007) Study of flow dynamics in complex vessels using doppler optical coherence tomography. Meas Sci Technol 18:3279–3286. doi:10.1088/0957-0233/18/11/003

Bounoua S, Lemaire E, Férec J, Ausias G, Kuzhir P (2016) Shear-thinning in concentrated rigid fiber suspensions: aggregation induced by adhesive interactions. J Rheol 60:1279–1300. doi:10.1122/1.4965431

Bukowska DM, Derzsi L, Tamborski S, Szkulmowski M, Garstecki P, Wojtkowski M (2013) Assessment of the flow velocity of blood cells in a microfluidic device using joint spectral and time domain optical coherence tomography. Opt Express 21:24025–24038. doi:10.1364/OE.21.024025

Chen P, Yu H, Liu Y, Chen W, Wang X, Ouyang M (2013) Concentration effects on the isolation and dynamic rheological behavior of cellulose nanofibers via ultrasonic processing. Cellulose 20:149–157. doi:10.1007/s10570-012-9829-7

Cheng DC (1986) Yield stress: a time-dependent property and how to measure it. Rheol Acta 25:542–554. doi:10.1007/BF01774406

Cloitre M, Bonnecaze R (2017) A review on wall slip in high solid dispersions. Rheol Acta 56:283–305. doi:10.1007/s00397-017-1002-7

Czajkowski J, Vilmi P, Lauri J, Sliz R, Fabritius T, Myllyla R (2012) Characterization of ink-jet printed RGB color filters with spectral domain optical coherence tomography. In Proc SPIE 8493:849308. doi:10.1117/12.929681

AQ2

Derakhshandeh B, Hatzikiriakos SG, Bennington CPJ (2010) The apparent yield stress of pulp fiber suspensions. J Rheol 54:1137–1154. doi:10.1122/1.3473923

Dimic-Misic K, Gane PAC, Paltakari J (2013) Micro- and nanofibrillated cellulose as a rheology modifier additive in CMC-containing pigment-coating formulations. Ind Eng Chem Res 52:16066–16083. doi:10.1021/ie4028878

Dimic-Misic K, Rantanen J, Maloney TP, Gane P (2016) Gel structure phase behavior in micro nanofibrillated cellulose containing in situ precipitated calcium carbonate. J Appl Polym Sci 133:43486. doi:10.1002/app.43486 **(1 of 13)**

Haavisto S, Liukkonen J, Jäsberg A, Koponen A, Lille M, Salmela J (2011) Laboratory-scale pipe rheometry: a study of a microfibrillated cellulose suspension. In: Proceedings of papercon 2011

AQ3

Haavisto S, Salmela J, Jäsberg A, Saarinen T, Karppinen A, Koponen A (2015) Rheological characterization of microfibrillated cellulose suspension using optical coherence tomography. Tappi J 14:291–302

Harvey M, Waigh TA (2011) Optical coherence tomography velocimetry in controlled shear flow. Phys Rev E 83:031502. doi:10.1103/PhysRevE.83.031502

Hoeng F, Denneulin A, Bras J (2016) Use of nanocellulose in printed electronics: a review. Nanoscale 8:13131–13154. doi:10.1039/C6NR03054H

Huang D, Swanson E, Lin C, Schuman J, Stinson W, Chang W, Hee M, Flotte T, Gregory K, Puliafito C, Fujimoto J (1991) Optical coherence tomography. Science 254:1178–1181. doi:10.1126/science.1957169

Iotti M, Gregersen ØW, Moe S, Lenes M (2011) Rheological studies of microfibrillar cellulose water dispersions. J Polym Environ 19:137–145. doi:10.1007/s10924-010-0248-2

Jaradat S, Harvey M, Waigh TA (2012) Shear-banding in polyacrylamide solutions revealed via optical coherence tomography velocimetry. Soft Matter 8:11677–11686. doi:10.1039/C2SM26395E

Jia Y, Bagnaninchi PO, Yang Y, Haj AE, Hinds MT, Kirkpatrick SJ, Wang RK (2009) Doppler optical coherence tomography imaging of local fluid flow and shear stress within microporous scaffolds. J Biomed Opt 14:034014–034014. doi:10.1117/1.3130345

Jonoobi M, Oladi R, Davoudpour Y, Oksman K, Dufresne A, Hamzeh Y, Davoodi R (2015) Different preparation methods and properties of nanostructured cellulose from various natural resources and residues: a review. Cellulose 22:935–969. doi:10.1007/s10570-015-0551-0

Kalia S, Boufi S, Celli A, Kango S (2014) Nanofibrillated cellulose: surface modification and potential applications. Colloid Polym Sci 292:5–31. doi:10.1007/s00396-013-3112-9

Karppinen A, Saarinen T, Salmela J, Laukkanen A, Nuopponen M, Seppälä J (2012) Flocculation of microfibrillated cellulose in shear flow. Cellulose 19:1807–1819. doi:10.1007/s10570-012-9766-5

Kumar V, Nazari B, Bousfield D, Toivakka M (2016) Rheology of microfibrillated cellulose suspensions in pressure-driven flow. Appl Rheol 26:43534. doi:10.3933/ApplRheol-26-43534

Lasseuguette E, Roux D, Nishiyama Y (2008) Rheological properties of microfibrillar suspension of TEMPO-oxidized pulp. Cellulose 15:425–433. doi:10.1007/s10570-007-9184-2

Lauri J, Bykov AV, Myllyla R (2011a) Determination of suspension viscosity from the flow velocity profile measured by Doppler Optical Coherence Tomography. Photon Lett Poland 3:82–84. doi:10.4302/plp.2011.2.13

Lauri J, Bykov AV, Priezzhev AV, Myllylä R (2011b) Experimental study of the multiple scattering effect on the flow velocity profiles measured in Intralipid phantoms by DOCT. Laser Phys 21:813–817. doi:10.1134/S1054660X11070164

Lauri J, Czajkowski J, Myllylä R, Fabritius T (2015) Measuring flow dynamics in a microfluidic chip using optical coherence tomography with 1 μm axial resolution. Flow Meas Instrum 43:1–5. doi:10.1016/j.flowmeasinst.2015.02.001

Lavoine N, Desloges I, Dufresne A, Bras J (2012) Microfibrillated cellulose–its barrier properties and applications in cellulosic materials: a review. Carbohydr Polym 90:735–764. doi:10.1016/j.carbpol.2012.05.026

Markstedt K, Mantas A, Tournier I, Martínez Ávila H, Hägg D, Gatenholm P (2015) 3D Bioprinting human chondrocytes with nanocellulose–alginate bioink for cartilage tissue engineering applications. Biomacromolecules 16:1489–1496. doi:10.1021/acs.biomac.5b00188

Martoïa F, Perge C, Dumont PJJ, Orgeas L, Fardin MA, Manneville S, Belgacem MN (2015) Heterogeneous flow kinematics of cellulose nanofibril suspensions under shear. Soft Matter 11:4742–4755. doi:10.1039/C5SM00530B

Metzner AB, Reed JC (1955) Flow of non-Newtonian fluids—correlation of the laminar, transition, and turbulent-flow regions. AIChE J 1:434–440. doi:10.1002/aic.690010409

Missoum K, Belgacem NM, Bras J (2013) Nanofibrillated cellulose surface modification: a review. Materials 6:1745–1766. doi:10.3390/ma6051745

Moberg T, Sahlin K, Yao K, Geng S, Westman G, Zhou Q, Oksman K, Rigdahl M (2017) Rheological properties of nanocellulose suspensions: effects of fibril/particle dimensions and surface characteristics. Cellulose 24:2499–2510. doi:10.1007/s10570-017-1283-0

Moger J, Matcher SJ, Winlove CP, Shore A (2004) Measuring red blood cell flow dynamics in a glass capillary using Doppler optical coherence

tomography and Doppler amplitude optical coherence tomography. J Biomed Optics 9:982–994. doi:10.1117/1.1781163

Mykhaylyk OO, Warren NJ, Parnell AJ, Pfeifer G, Laeuger J (2016) Applications of shear-induced polarized light imaging (SIPLI) technique for mechano-optical rheology of polymers and soft matter materials. J Polym Sci, Part B: Polym Phys 54:2151–2170. doi:10.1002/polb.24111

Naderi A, Lindström T (2015) Rheological measurements on nanofibrillated cellulose systems: a science in progress. In: Mondal MIH (ed) Cellulose and cellulose derivatives: synthesis, modification and applications. Nova Science Publishers, New York

Nazari B, Kumar V, Bousfield D, Toivakka M (2016) Rheology of cellulose nanofibers suspensions: boundary driven flow. J Rheol 60:1151–1159. doi:10.1122/1.4960336

Nechyporchuk O, Belgacem MN, Pignon F (2014) Rheological properties of micro-/nanofibrillated cellulose suspensions: wall-slip and shear banding phenomena. Carbohydr Polym 112:432–439. doi:10.1016/j.carbpol.2014.05.092

Olmsted PD (2008) Perspectives on shear banding in complex fluids. Rheol Acta 47:283–300. doi:10.1007/s00397-008-0260-9

Osong SH, Norgren S, Engstrand P (2016) Processing of wood-based microfibrillated cellulose and nanofibrillated cellulose, and applications relating to papermaking: a review. Cellulose 23:93–123. doi:10.1007/s10570-015-0798-5

Pääkkö M, Ankerfors M, Kosonen H, Nykänen A, Ahola S, Österberg M, Ruokolainen J, Laine J, Larsson PT, Ikkala O, Lindström T (2007) Enzymatic hydrolysis combined with mechanical shearing and high-pressure homogenization for nanoscale cellulose fibrils and strong gels. Biomacromolecules 8:1934–1941. doi:10.1021/bm061215p

Petrich MP, Koch DL, Cohen C (2000) An experimental determination of the stress–microstructure relationship in semi-concentrated fiber suspensions. J Non Newtonian Fluid Mech 95:101–133. doi:10.1016/S0377-0257(00)00172-5

Raiskinmäki P, Kataja M (2005) Disruptive shear stress measurements of fibre suspension using ultrasound Doppler techniques. Ann Trans The Nordic Rheol Soc 13:207–211

Robles FE, Wilson C, Grant G, Wax A (2011) Molecular imaging true-colour spectroscopic optical coherence tomography. Nat Photon, 5:744–747. doi: http://www.nature.com/nphoton/journal/v5/n12/abs/nphoton.2011.257.html#supple information

Saarinen T, Haavisto S, Sorvari A, Salmela J, Seppälä J (2014) The effect of wall depletion on the rheology of microfibrillated cellulose water suspensions by optical coherence tomography. Cellulose 21:1261–1275. doi:10.1007/s10570-014-0187-5

Salmela J, Haavisto S, Koponen A, Jäsberg A, Kataja M (2013) Rheological characterization of micro-fibrillated cellulose fibre suspension using multi scale velocity profile measurements. In: Proceedings of 15th fundamental research symphosium

Shao Y, Chaussy D, Grosseau P, Beneventi D (2015) Use of microfibrillated cellulose/lignosulfonate blends as carbon precursors: impact of hydrogel rheology on 3D printing. Ind Eng Chem Res 54:10575–10582. doi:10.1021/acs.iecr.5b02763

Siró I, Plackett D (2010) Microfibrillated cellulose and new nanocomposite materials: a review. Cellulose 17:459–494. doi:10.1007/s10570-010-9405-y

Sorvari A, Saarinen T, Haavisto S, Salmela J, Vuoriluoto M, Seppälä J (2014) Modifying the flocculation of microfibrillated cellulose suspensions by soluble polysaccharides under conditions unfavorable to adsorption. Carbohydr Polym 106:283–292. doi:10.1016/j.carbpol.2014.02.032

Swerin A, Ödberg L, Lindström T (1990) Deswelling of hardwood kraft pulp fibers by cationic polymers. Nord Pulp Pap Res J 5:188–196. doi:10.3183/NPPRJ-1990-05-04-p188-196

Vesterinen A, Myllytie P, Laine J, Seppälä J (2010) The effect of water-soluble polymers on rheology of microfibrillar cellulose suspension and dynamic mechanical properties of paper sheet. J Appl Polym Sci 116:2990–2997. doi:10.1002/app.31832

Wang RK (2004) High-resolution visualization of fluid dynamics with Doppler optical coherence tomography. Meas Sci Technol 15:725–733. doi:10.1088/0957-0233/15/4/016

Wang XJ, Milner TE, Nelson JS (1995) Characterization of fluid flow velocity by optical Doppler tomography. Opt Lett 20:1337–1339. doi:10.1364/OL.20.001337

Wang L, Wang Y, Guo S, Zhang J, Bachman M, Li GP, Chen Z (2004a) Frequency domain phase-resolved optical Doppler and Doppler variance tomography. Opt Commun 242:345–350. doi:10.1016/j.optcom.2004.08.035

Wang L, Xu W, Bachman M, Li G, Chen Z (2004b) Phase-resolved optical Doppler tomography for imaging flow dynamics in microfluidic channels. Appl Phys Lett 85:1855–1857. doi:10.1063/1.1785854

Wiklund JA, Stading M, Pettersson AJ, Rasmuson A (2006) A comparative study of UVP and LDA techniques for pulp suspensions in pipe flow. AIChE J 52:484–495. doi:10.1002/aic.10653

Yadav R, Lee K, Rolland JP, Zavislan JM, Aquavella JV, Yoon G (2011) Micrometer axial resolution OCT for corneal imaging. Biomed Opt Express 2:3037–3046. doi:10.1364/BOE.2.003037

Yang VXD, Gordon ML, Seng-Yue E, Lo S, Qi B, Pekar J, Mok A, Wilson BC, Vitkin IA (2003) High speed, wide velocity dynamic range Doppler optical coherence tomography (Part II): imaging in vivo cardiac dynamics of Xenopus laevis. Opt Express 11:1650–1658. doi:10.1364/OE.11.001650

Zhao Y, Chen Z, Saxer C, Xiang S, de Boer JF, Nelson JS (2000) Phase-resolved optical coherence tomography and optical Doppler tomography for imaging blood flow in human skin with fast scanning speed and high velocity sensitivity. Opt Lett 25:114–116. doi:10.1364/OL.25.000114